Sixth International Symposium on Marine Propulsors
smp'19, Rome, Italy, May 2019

CFD Analysis of Ship Propeller Thrust Breakdown

Keun Woo Shin[1], Poul Andersen[2]

[1]Propeller & Aftship R&D Department, MAN Energy Solutions, Frederikshavn, Denmark
[2]Department of Mechanical Engineering (MEK), Technical University of Denmark (DTU), Kgs. Lyngby, Denmark

ABSTRACT

The variation of propeller performance with respect to cavity extent over the blade surface is investigated by DES with a cavitation model. INSEAN E779A propeller is considered as a test case, because the cavitation tunnel test results of thrust and torque breakdowns with respect to cavitation number and cavity extent are available for several loading conditions (Pereira et al 2004a).

Cavitation simulation results are validated against the experimental result at two cavitation numbers in the highest loading condition among those considered in the experiment. In the validation, the effects of the transition model and the seed density on cavity extent and propeller performance are examined and the propeller inflow is adjusted to reach the measured thrust instead of modeling the blockage effect of the cavitation tunnel.

Cavitation simulations are made with varying cavitation number. The comparison of the CFD and experimental results shows a reasonable agreement in the variations of cavity extent, thrust and torque in moderate cavitation. Thrust and torque breakdowns are simulated at higher cavitation numbers and larger cavity extents in CFD, as cavity area is overestimated especially in extensive cavitation.

Keywords

Thrust breakdown, cavitation, CFD, INSEAN E779A, DES

1 INTRODUCTION

Thrust breakdown and propulsive efficiency loss driven by extensive cavitation are not direct concerns in propeller designs of general merchant ships nowadays, because sheet cavity extents can be constrained by using propeller design programs and significant alterations of propeller performance are reckoned to be avoided. Since some degree of cavitation is unavoidable in actual ship propeller operations and it can be intensified in off-design conditions or high ocean waves, evaluations of propeller performance with considering thrust breakdown under cavitating conditions are necessary.

When cavitation is not widely formed over the blade surface near the initial cavitation inception, thrust and torque can increase slightly over those in the non-cavitating condition. When cavitation is formed up to 5 – 10% of the suction-side blade surface, thrust breakdown can be avoided according to the Burrill diagram often used for determining the blade area ratio in the preliminary propeller design phase (Burrill & Emerson 1963). When the blade section is modified from standard airfoil sections for delaying the cavitation onset and thrust breakdown, cavitation can be more extended up to 15% of the suction-side blade surface without thrust breakdown (Black 2007). More than 1 – 2% reduction of thrust compared to that in the fully wetted condition is often referred to as thrust breakdown.

Potential flow solvers like boundary element method (BEM) are still workhorse tools commonly adopted for optimizing propeller designs with respect to propulsive efficiency and cavitation safety. BEM with a cavitation model can predict a general trend of thrust loss in cavitating conditions, but it is conservative to overestimate thrust loss and to show a higher critical cavitation number leading to thrust breakdown than the experiment (Pereira et al 2004a, Black 2007).

The accuracy and robustness of CFD made by turbulent viscous flow solvers like RANS, DES and LES are generally known to be better in predicting propeller performance and simulating cavitating flows than those of potential flow solvers. CFD methods have been validated against cavitation tunnel test results for predicting unsteady cavitation on a propeller installed on a hull model or in a hull wake field (Bensow & Bark 2010, Paik et al 2013). CFD has been improved to simulate different complex types of cavitation like cloud and tip vortex cavitation as well as attached sheet cavitation (Shin & Andersen 2018a, Yilmaz et al 2018).

Most validations of CFD simulations are focused on predicting extents of sheet cavitation attached to the blade surface, but there have been few validating works for thrust breakdown. Steady RANS simulations for cavitating flows on a ship propeller have shown a good agreement with an experimental result in predicting the critical cavitation number inducing thrust breakdown, but the quantitative prediction of thrust loss in cavitating conditions has had deviation from the experimental result (Lindau et al 2005).

In this work, the variations of cavity extent, thrust and torque are investigated by unsteady simulations made by a DES solver with a cavitation model. The numerical analysis of pressure and flow fields is made in cavitating conditions leading to thrust breakdown. The adopted CFD approach has been validated against the results of cavitation tunnel tests on ship propellers (Shin et al 2015, Shin & Andersen 2018b).

INSEAN E779A propeller is considered as a test case, because the experimental results of thrust and torque breakdowns with respect to cavitation number and cavity extent are available for several loading conditions (Pereira et al 2004a) and cavitation simulations have been attempted by different institutes (Salvatore et al 2009, Bensow & Bark 2010).

The variation of propeller performance with respect to the cavity extent over the blade area is investigated by using DES with a multi-phase flow model, which is an up-to-date method for cavitation simulation and has been validated against cavitation tunnel test results for different types of propeller cavitation (Shin et al 2015, Shin & Andersen 2015, Shin & Andersen 2018a).

Cavitation simulations at different cavitation numbers in the open-water condition are validated against the experimental results with respect to cavity extent, thrust and torque. As cavitation simulations of multiple institutes have had difficulty in reproducing the extent of sheet cavitation accurately especially at a low cavitation number (Vaz et al 2015), the investigation is focused on assessing the CFD accuracy in estimating the variations of thrust and torque with respect to the cavity area over the blade surface. The cause of the thrust breakdown is investigated by looking into the spanwise distribution of axial loadings from viscous shear stress and remaining pressure and sectional pressure distributions in outer radii in conditions with different cavity extents.

2 TEST CASE

The INSEAN E779A propeller considered as a test case is a 4-bladed propeller designed for a twin-screw ferry. The model propeller diameter is D = 227.3 mm. It has a forward rake and the blade sections have flat pressure-side contours as a modification of Wageningen B-series propeller. The rake angle of 4.6° and the skew angle of 4.8° at the tip are smaller than those of the B-series propeller. It has a uniform pitch ratio of P/D = 1.1 and 68.9% expanded area ratio (Salvatore 2006).

A comprehensive series of experiments have been conducted on this propeller in cavitating and non-cavitating conditions with visualizing propeller wake fields and measuring cavity patterns, pressure pulses and acoustic noise. As the experimental results provide a quantitative data set for the validation of numerical methods, it has been considered by a number of research institutes working on the development of numerical models for simulating propeller flows.

The cavitation test results in both the open-water and behind-hull conditions are available (Pereira et al 2004b), but only the open-water cavitating condition is considered in this work, because cavitation variation is small in the open-water condition and so it is convenient to investigate the correlation between cavity extent and thrust variation. Open-water cavitation tests have been made in an extensive range of propeller loadings and cavity extents corresponding to advance ratios of J = 0.65 – 0.88 and cavitation numbers of σ_n = 0.4 – 3.4, where $J = V_A/(N{\cdot}D)$ and $\sigma_n = (P_O{-}P_V)/(0.5{\cdot}\rho{\cdot}N^2{\cdot}D^2)$. The variations of cavity extent, thrust and torque with respect to σ_n have been examined at J = 0.71, 0.77, 0.83 in the experiment. The highest loading condition of J = 0.71 among the three advance ratios is considered.

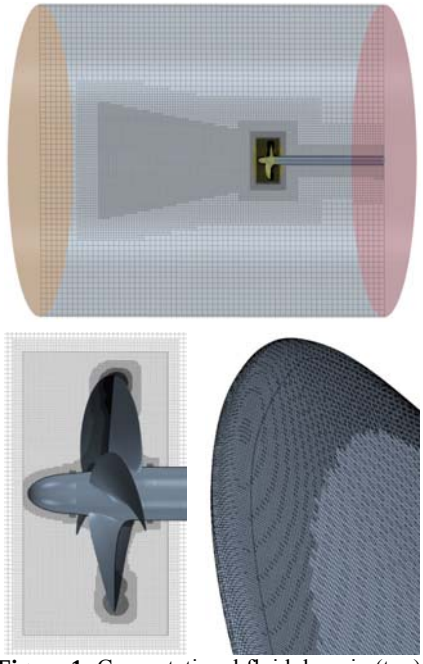

Figure 1: Computational fluid domain (top), volume grid around the propeller model (bottom left) and surface grid on the blade tip (bottom right)

3 CFD SETUP

Unsteady cavitation simulations are made by adopting a DES solver in the commercial CFD software StarCCM+ with curvature-corrected k-ω SST turbulence and γ-Re_θ transition model. DES is used rather than RANS simulations for resolving flow separation better at the closure region of extensive sheet cavitation. Two-phase flows are modelled by the volume-of-fluid (VOF) method and a generic transport equation for vapor volume fraction α. Cavitation is modelled by the interphase mass transfer model of Schnerr & Sauer (2001). In the cavitation model, spherical seeds accounting for solid particles and dissolved gas in the experimental condition are assumed to be uniformly distributed with constant density and initial radius in the liquid domain. Cavitation is initiated by the increase of bubble radius from the initial seed radius governed by the asymptotic Rayleigh-Plesset equation. The change rate of α is dependent on the seed density n_O and the initial seed radius as well as the bubble radius variation. The effect of n_O on cavity extent and

sectional pressure distribution is examined in the following validation of cavitation simulations.

A trimmed hexahedral grid is prepared around the propeller model with an upstream shaft in a cylindrical fluid domain extending $3{\cdot}D$ from the propeller plane to the inlet, $6{\cdot}D$ to the outlet and $4{\cdot}D$ radially to the outer wall, as shown in Figure 1. The cross-section area of the computational domain is much larger than that of the cavitation tunnel with 0.6 m square section and the outer wall and upstream shaft have a slip boundary condition, so the blockage effect of the cavitation tunnel is not taken into account in the CFD setup. Instead, J in CFD is altered from the specified value by adjusting the inflow speed V_A to reach the measured value of K_T from the experiment. The propeller speed N is fixed to $N = 36.0$ rps by following the computational setup in Vaz et al (2015). Propeller rotations are modelled by the rigid body motion and the sliding grid in a sub-domain around the propeller model.

The grid size is 0.2 – 0.5 mm on the blade surface and it is refined to 0.1 – 0.3 mm on the patches at the blade edge for resolving high curvature. The blade geometry is separated into the suction and pressure sides and there are also separate patches along the blade edge, so the refined region can be readily defined. The region near the outer-radius blade surface of $0.7{\cdot}R$ – $1.0{\cdot}R$ is set to have a fine volumetric grid of Δx = 0.3 – 0.4 mm for resolving cavitating flows better. The grid at the wall boundary has 12 prism layers leading to non-dimensional first-cell heights mostly of $y+ \leq 1$. The time step corresponds to 0.5° propeller rotation per Δt and a 2nd-order implicit time-stepping scheme is used.

4 CFD VALIDATION

Cavitation simulations are validated against the experimental result. As high-quality photos from the experiment are available at σ_n = 0.630, 1.763 (Salvatore 2006), these two cavitation numbers are considered in the validation. Since the discrepancy of cavitation simulations from the experimental result is often deemed to be related to water quality of cavitation tunnel and laminar & transitional flows, the effects of seed density and transition model on the CFD results are investigated.

CFD at $J = 0.71$ and $\sigma_n = 1.763$ shows 7.3% lower thrust than in the experiment, because the cavitation tunnel blockage effect is not included in the CFD. The experimental measurement shows $K_T = 0.255$ at σ_n = 1.262 – 2.780 showing moderate cavitation (Pereira et al 2004a). The inflow speed V_A in CFD is 4.2% lowered from that in the experiment to reach the measured thrust with 0.2% deviation. V_A in CFD adjusted once at σ_n = 1.763 is applied to the other simulations at different values of σ_n for investigating thrust breakdown in the next section.

The cavity interface in CFD is defined by two iso-surfaces of $\alpha = 0.1$ and 0.5. As the cavity of a larger vapor volume fraction exists inside that of a lower fraction, the iso-surfaces of α = 0.1 and 0.5 are plotted transparently with dark and light blue colors, respectively, in the following result presentations.

4.1 Open-water Curve Without Cavitation

Before starting cavitation simulations, CFD is validated against the open-water propeller test result in fully wetted flows. CFD is made in the same setup as for cavitation simulations, but steady simulations are made with excluding the cavitation model. The comparison of the open-water curves in Figure 2 shows overall underestimations of CFD in K_T and K_Q. The deviations from the experimental result are 0.6 – 2.5% in K_T and 2.6 – 4.6% in K_Q at J = 0.1 – 0.7. As the underestimations in K_Q are larger than in K_T, the open-water efficiency η_O is overestimated by 2.1 – 3.3%.

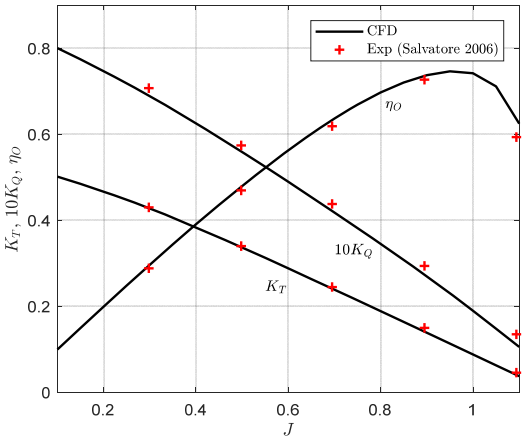

Figure 2: Open-water curves in CFD and the experiment without cavitation

4.2 Seed Density

Cavitation simulations are made with varying the seed density in the range of $n_O = 10^6 – 10^{10}$. The cavity extents in CFD for different n_O are compared with the experimental results in Figure 3 – 4. The chordwise cavity extent at $\sigma_n = 1.763$ is larger for higher n_O. The chordwise extent of the sheet cavity especially at r/R = 0.9 – 1.0 is overestimated by CFD for $n_O \geq 10^8$ and the conversion to tip vortex cavitation occurs more downstream from the blade tip than in the experiment. The leading-edge cavitation starts from r/R = 0.6 – 0.7 in CFD and the radial starting point does not change significantly for $n_O \geq 10^8$, whereas it starts at a more outer radius of $r/R > 0.7$ in the experiment.

In Figure 5, the distributions of pressure coefficient C_P on constant-radius sections of $r/R = 0.7$ and 0.9 are compared in CFD for different n_O, where $C_P = (P–P_\infty)/(0.5{\cdot}\rho{\cdot}N^2{\cdot}D^2)$ and P_∞ is the ambient pressure. When there is a short cavity at r/R = 0.7 for $n_O = 10^6 – 10^8$, the minimum pressure at the leading edge of the suction side is not changed so much, as shown in Figure 5(a). When the cavity at $r/R = 0.7$ is extended for $n_O = 10^{10}$, the leading-edge suction peak is lowered and a constant pressure at the saturation pressure is extended over $x/C = 0.2$. The leading-edge minimum pressure at $r/R = 0.9$ is $–C_P = 10.0$ for $n_O = 10^6$ and it is lowered to $–C_P = 5.3$ and 4.0 and the

constant pressure region is extended to $x/C = 0.5$ and 0.88 for $n_O = 10^8$ and 10^{10}, respectively.

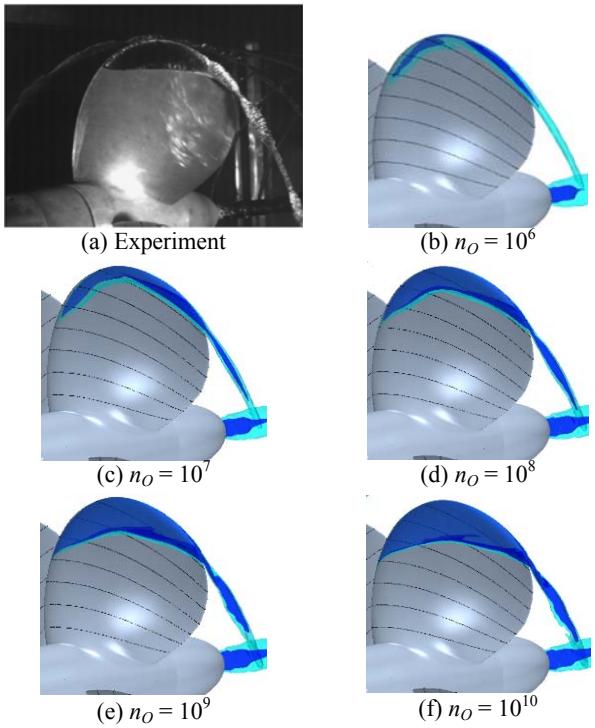

(a) Experiment (b) $n_O = 10^6$ (c) $n_O = 10^7$ (d) $n_O = 10^8$ (e) $n_O = 10^9$ (f) $n_O = 10^{10}$

Figure 3: Cavity extents from the experiment (Salvatore 2006) and CFD with varying seed density at $J = 0.71$, $\sigma_n = 1.763$ (Blue – $\alpha = 0.5$, Light blue – $\alpha = 0.1$)

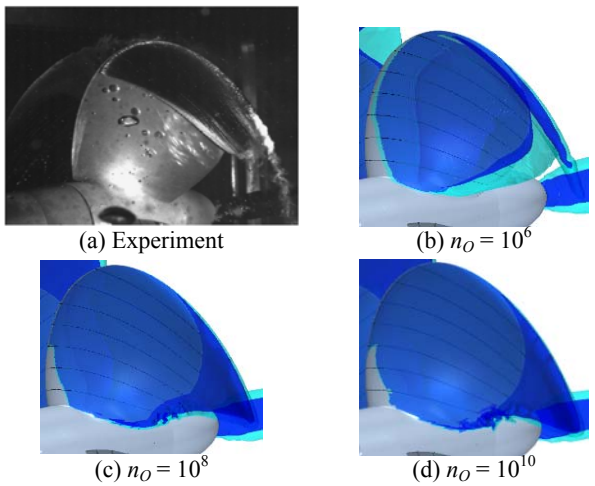

(a) Experiment (b) $n_O = 10^6$ (c) $n_O = 10^8$ (d) $n_O = 10^{10}$

Figure 4: Cavity extents from the experiment (Salvatore 2006) and CFD with varying seed density in $J = 0.71$, $\sigma_n = 0.630$ (Blue – $\alpha = 0.5$, Light blue – $\alpha = 0.1$)

While the CFD result in Figure 4 shows cavitation all over the suction side of the blade except the leading edge of $r/R \leq 0.5$ at $\sigma_n = 0.630$, the experiment shows supercavitation at $r/R \geq 0.7$ and bubble cavitation at $r/R < 0.7$. The cavity extent over the trailing edge is increased in CFD for higher n_O and the cavity area covering almost the whole suction-side blade surface is not changed significantly even for $n_O = 10^6$. CFD shows a distinct difference in the cavitation at $r/R < 0.7$ from the experiment, but the separation of the tip vortex cavitation from the supercavitation is reproduced in CFD for $n_O = 10^6$. Overestimations in the cavity extent at inner radii are commonly shown in other CFD validations for this case (Vaz et al 2015). As CFD for $n_O = 10^6$ shows a better agreement at $\sigma_n = 1.763$, the following simulations are made for this seed density.

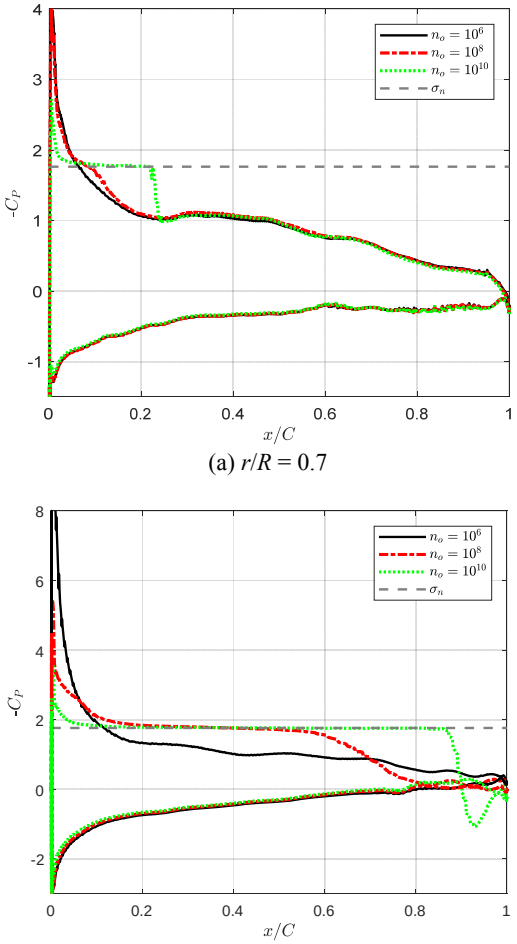

(a) $r/R = 0.7$ (b) $r/R = 0.9$

Figure 5: Sectional pressure distributions in CFD at $J = 0.71$, $\sigma_n = 1.763$ with varying seed density

4.3 Transition Model

Cavitation simulations are made with and without the transition model. Two cavitation numbers of $\sigma_n = 1.763$ and 10.0 are applied to CFD for considering cavitating and non-cavitating flows. Since most cavitation at $\sigma_n = 1.763$ occurs in the outer radii of $r/R \geq 0.7$ having fully turbulent flows, the comparison of cavity extents in CFD with and without the transition model shows little difference, as shown in Figure 6. However, K_T in CFD with the transition model is 1.8 – 1.9% higher than without it mostly due to lower viscous shear stress.

The spanwise distributions of axial loading in CFD with and without the transition model are compared in Figure 7. The blade surface is divided into 100 strips by cylindrical sections with a constant radial interval dt_{STR} and thrust is integrated on each strip to calculate dK_T. The integration of dK_T/dt_{STR} over the blade span is the same as K_T for the whole propeller blades. The total axial loading in CFD without the transition model is slightly lower all over the spanwise positions except near the tip in fully wetted flows. In Figure 7(b), the axial loading from viscous shear stress has an opposite direction to propeller

thrust and it is higher more than twice at some spanwise positions without the transition model in both the fully wetted and cavitating flows, which shows that the higher K_T in CFD with the transition model stems mainly from lower viscous shear stress. The difference in the spanwise loading distributions between the fully wetted and cavitating flows is discussed further in the following section.

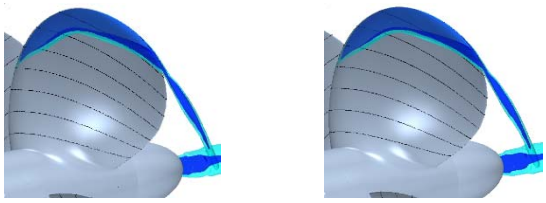

(a) With transition model (b) Without transition model

Figure 6: Cavity extents in CFD with and without the transition model in $J = 0.71$, $\sigma_n = 1.763$ (Blue – $\alpha = 0.5$, Light blue – $\alpha = 0.1$)

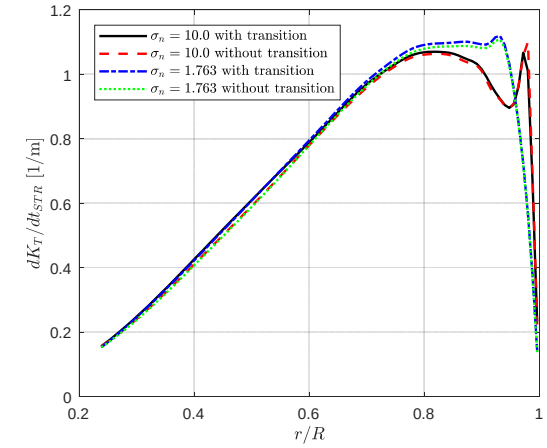

(a) Total axial loading

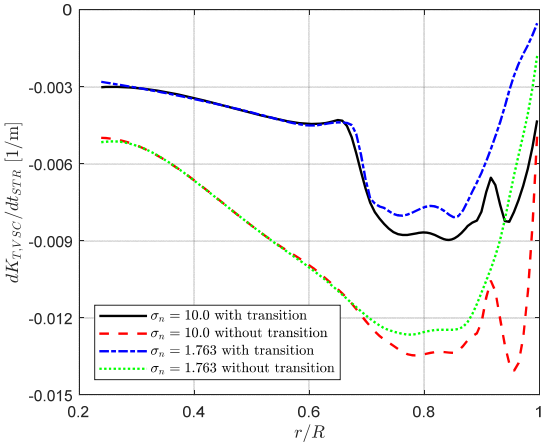

(b) Axial loading from viscous shear stress

Figure 7: Spawise distributions of axial loading in CFD with and without the transition model

In Figure 8, the surface-constrained streamlines and the skin friction coefficient C_F on the suction side of the blade are compared in CFD with and without the transition model, where $C_F = \tau_W/(0.5 \cdot \rho \cdot N^2 \cdot D^2)$ and τ_W is the wall shear stress. The sharp increase of C_F and the streamline pattern change at $r/R \approx 0.7$ show a clear separation of flow regimes in CFD for non-cavitating flows with the transition model. The streamlines along constant radii in the outer-radius region of $r/R \geq 0.7$ indicate fully turbulent flows and the diagonally outward streamlines in the inner radii of $r/R < 0.7$ indicate laminar flows from the leading edge over the mid-chord. The change of streamline direction seems to indicate a laminar-turbulent transition at $x/C = 0.7 – 0.8$ of $r/R = 0.5 – 0.7$. The radially outward deflection of streamlines indicates a laminar separation aft of $x/C = 0.6$ at $r/R \leq 0.5$. As a paint test on another model propeller (Kuiper 1981) shows similarities to Figure 8(a), CFD with the transition model seems to be better in simulating laminar-turbulent transitional boundary layer flows than without it.

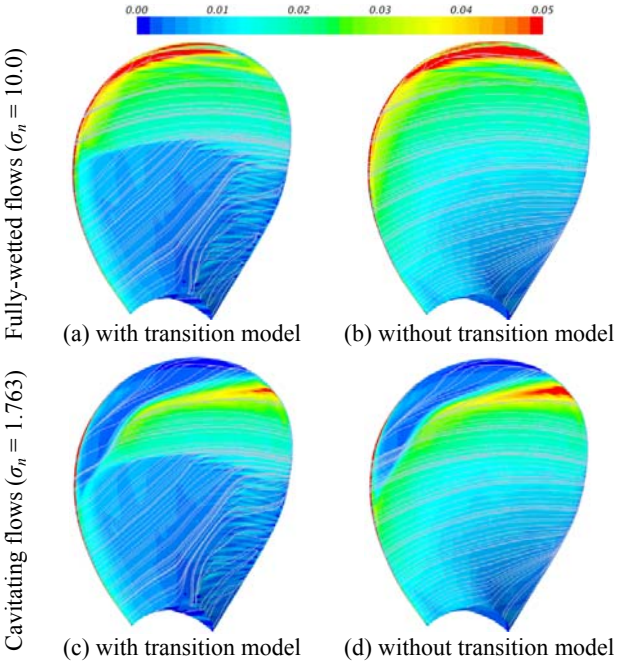

(a) with transition model (b) without transition model

(c) with transition model (d) without transition model

Figure 8: C_F with surface-constrained streamlines in CFD with and without the transition model

When the transition model is not included, C_F gradually increases from inner to outer radii and streamlines are along the tangential direction all over the blade surface. C_F along the leading edge and tip in the fully wetted flows and at the rear part of sheet cavity in the cavitating flows is higher in CFD without the transition model, which may be related to stronger vortices at the leading edge and the cavity closure. The region under the sheet cavity has low C_F commonly in both CFD with and without the transition model.

5 THRUST BREAKDOWN

Cavitation simulations are made with varying cavitation number in the range of $\sigma_N = 0.63 – 10.0$ for investigating the variations of cavity extent and propeller performance. In Figure 9, the variation of cavity extent shows that the cavitation at the leading and trailing edges of $r/R \leq 0.5$ is reduced to the mid-chord, when σ_N is increased from 0.63 to 1.0. Cavitation is shown only in the outer radii of $r/R \geq 0.6$ at $\sigma_N = 1.14$, which looks like the experimental result at $\sigma_N = 0.63$. As σ_N is increased from 1.14, the chordwise extent of the sheet cavitation is reduced and the cavitation is shown only in the leading-edge and tip region of $r/R \geq$

0.7 at $\sigma_N = 2.515$. As the supercavitation dwindles at $r/R \leq 0.95$ with the increase of σ_N from 1.14 to 1.763, tip vortex cavitation is formed and stabilized. The cavity at the leading edge and tip gradually diminishes with increasing σ_N from 1.763 and the weakened cavity at the tip fades completely at $\sigma_N = 7.0 – 10.0$.

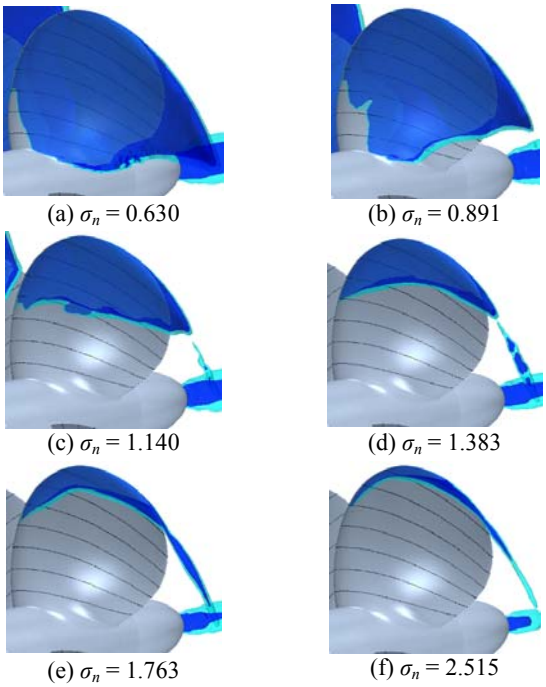

(a) $\sigma_n = 0.630$ (b) $\sigma_n = 0.891$ (c) $\sigma_n = 1.140$ (d) $\sigma_n = 1.383$ (e) $\sigma_n = 1.763$ (f) $\sigma_n = 2.515$

Figure 9: Cavity extent in CFD with respect to cavitation number in $J = 0.71$ (Blue – $\alpha = 0.5$, Light blue – $\alpha = 0.1$)

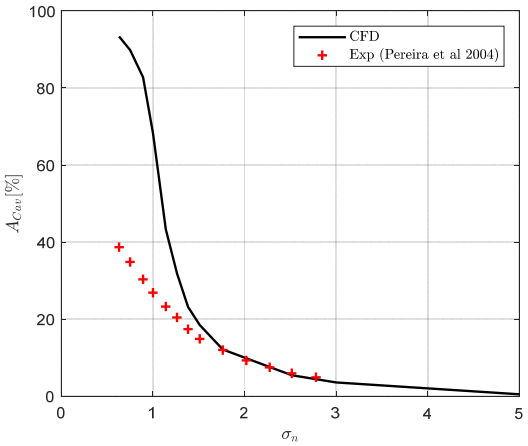

Figure 10: Cavity area ratio with respect to cavitation number in CFD and experiment

In Figure 10, the variation in cavity area ratio A_{CAV} with respect to σ_N is compared between CFD and the experiment. A_{CAV} is the ratio of the surface area under cavity to the suction-side blade area. The cavity area in CFD is defined by the blade surface area with $\alpha \geq 0.1$. CFD shows a good agreement in A_{CAV} and its gradient at $\sigma_N \geq 1.763$ having moderate sheet cavitation, although expanded surface areas are calculated for A_{CAV} in CFD and projected areas are measured in the experiment. Both CFD and the experiment show steeper slopes at lower cavitation numbers, but the slope in CFD is even steeper at $\sigma_N < 1.763$ and hence deviations are increased at lower cavitation numbers. As A_{CAV} is over 90% and cavitation is increased over the trailing edge in CFD, the slope does not get steeper at $\sigma_N \leq 0.891$.

The variations of K_T and K_Q in CFD and the experiment are presented with respect to σ_N in Figure 11. The variations of K_T in CFD and the experiment are within 1% at $\sigma_N \geq 1.262$ and $\sigma_N \geq 1.14$, respectively, although A_{CAV} is increased to 31.8% at $\sigma_N = 1.262$ in CFD and to 23.3% at $\sigma_N = 1.14$ in the experiment. K_T is reduced by over 2% at $\sigma_N \leq 1.14$ in CFD and at $\sigma_N \leq 1.0$ in the experiment and drops down more steeply at lower values of σ_N. As the cavity area is overestimated, the K_T drops in low σ_N are also larger in CFD than in the experiment.

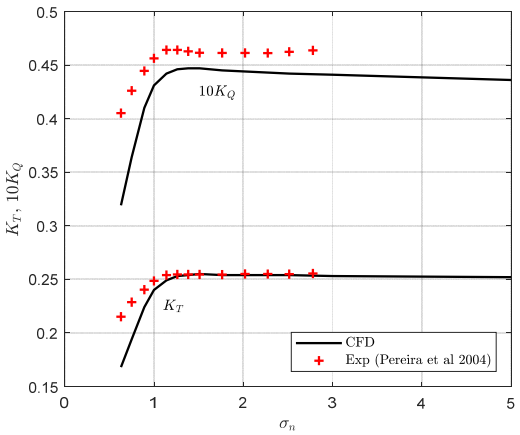

Figure 11: K_T and K_Q with respect to cavitation number in CFD and experiment

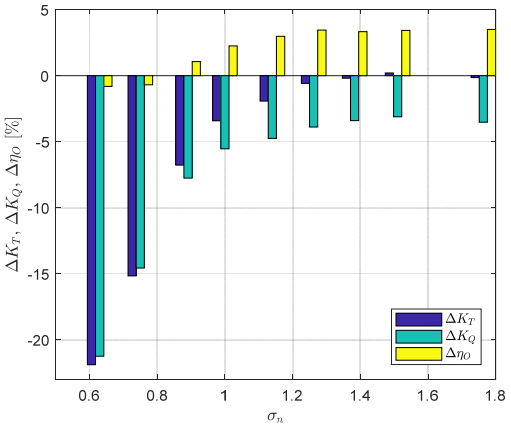

Figure 12: CFD deviations from the experimental result in K_T, K_Q and η_O with respect to cavitation number ($\Delta\phi = \phi_{CFD}/\phi_{EXP} - 1$)

K_Q in CFD is increased by 3% in moderate cavitation with decreasing σ_N from 10.0 to 1.51, whereas the K_Q variation in the experiment is within 1% at $\sigma_N = 1.14 – 2.78$. The breakdowns of K_Q in both CFD and the experiment are shown at lower σ_N than those of K_T, so the propeller efficiency η_O is lowered. The K_Q slope at $\sigma_N \leq 1.0$ looks steeper than for K_T, but the relative reductions of K_Q at $\sigma_N \leq 1.14$ are smaller than those of K_T, which leads to efficiency losses in extensive cavitation at low σ_N.

The deviations of CFD from the experimental result in K_T are within 1% at $\sigma_N = 1.262 – 2.515$ as shown in Figure 12, because the inflow speed in CFD is adjusted to reach

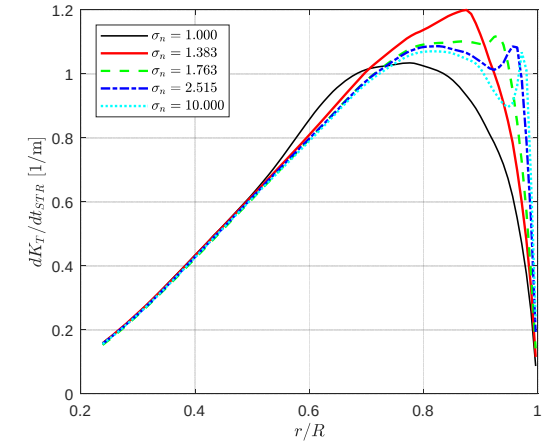

(a) Total axial loading

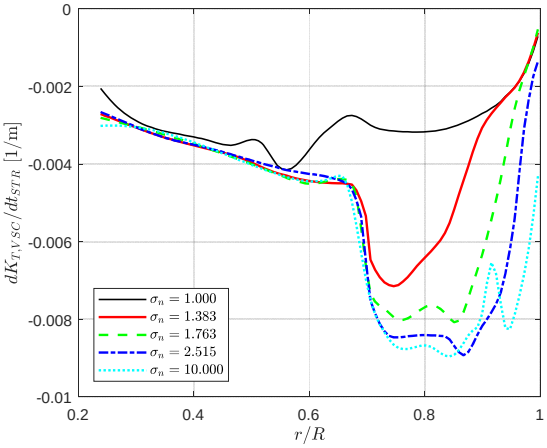

(b) Axial loading from viscous shear stress

Figure 13: Spawise distributions of axial loading for different cavitation numbers

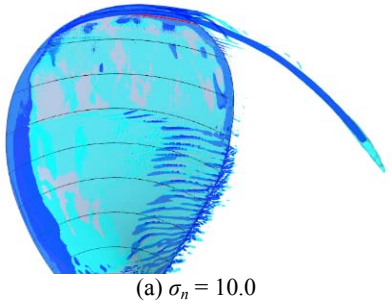

(a) $\sigma_n = 10.0$

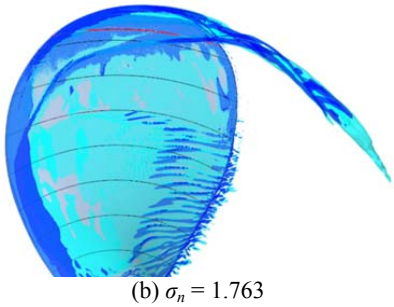

(b) $\sigma_n = 1.763$

Figure 14: Iso-surface of Q-criterion (Blue – $Q = 10^7$, Light blue – $Q = 5{\cdot}10^6$, Red line – Radial position of sharp peak in spanwise loading distribution)

the measured thrust at $\sigma_N = 1.763$. K_Q is underestimated by 3.1 – 4.8% at $\sigma_N = 1.14 – 2.515$ in CFD, as K_Q has larger underestimations than K_T in the open-water CFD validation without cavitation. As the deviations in both K_T and K_Q are increased to similar levels in extensive cavitation at $\sigma_N \leq 0.891$, the deviations in η_O are reduced to less than 1.1%.

The spanwise distributions of axial loading at different cavitation numbers are compared in Figure 13. In the non-cavitating condition of $\sigma_N = 10.0$, the axial loading is gradually increased from inner radii to $r/R = 0.82$ and decreased from the top to $r/R = 0.95$. It bounces up at $r/R = 0.95$ and makes a sharp peak at $r/R = 0.97$ and a fall-off to the tip. As the dip between the two peaks in the axial loading distribution goes up at $\sigma_N = 2.515$, K_T at $\sigma_N = 2.515$ is 1.3% higher than at $\sigma_N = 10.0$.

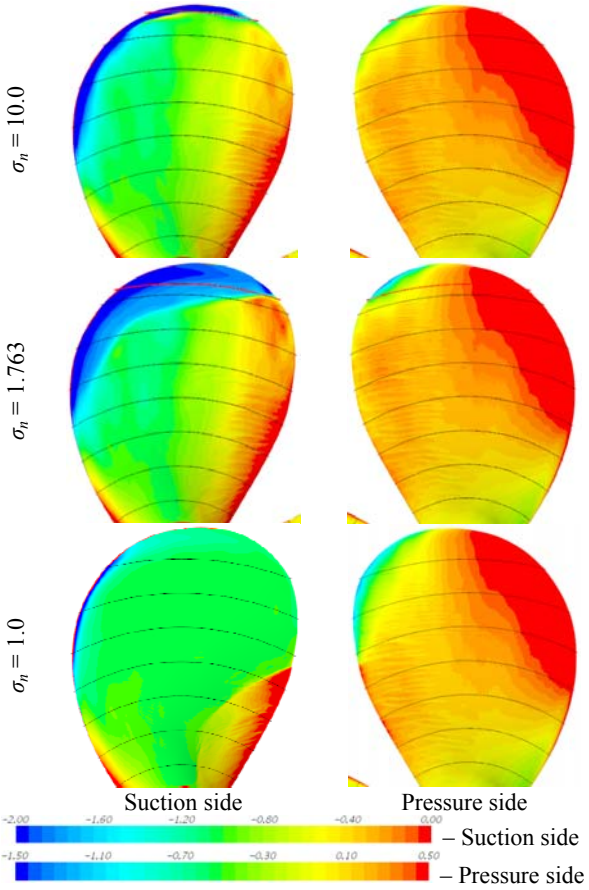

Figure 15: C_P on the blade surface in the fully wetted and cavitating flows (Red line – Radial position of sharp peak in spanwise loading distribution)

Even though K_T varies within 0.4% at $\sigma_N = 1.383 – 2.515$, the axial loading distributions have distinct differences in the cavitating region of $r/R \geq 0.7$. As the cavity extent is increased with reducing σ_N from 2.515 to 1.763, the sharp peak is moved from $r/R = 0.96$ to 0.93 and the dip between the two peaks is flattened. As the two peaks are merged at $\sigma_N = 1.383$, the maximum loading is raised with a downslope from $r/R = 0.88$. As cavitation is all over the outer-radius region of $r/R \geq 0.65$ at $\sigma_N = 1.0$, the maximum loading is lowered with a gradual drop-down from $r/R = 0.77$.

The iso-surfaces of Q-criterion in Figure 14 show that tip vortex is thicker in the cavitating condition of $\sigma_N = 1.763$ than without cavitation at $\sigma_N = 10.0$ and so the sharp peak

in the axial loading distribution is moved from r/R = 0.97 to 0.93. The radial position of the sharp peak marked by the red line is right below the tip vortex.

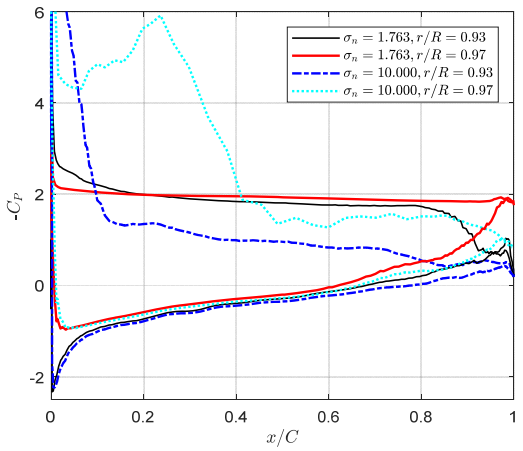

Figure 16: Sectional pressure distributions in CFD on r/R = 0.93 and 0.97 at σ_n = 1.763 and 10.0

The surface pressure distributions in Figure 15 show that in the tip region C_P on the pressure side is lowered at the trailing edge. While the region with the lowered pressure matches well the radial positions of r/R = 0.97 – 1.0 from the sharp loading peak indicated by the red line outwards with the loading fall-off at σ_N = 1.763, it matches the positions of r/R = 0.85 – 1.0 not from the sharp peak but from the first round top at σ_N = 10.0. It extends to r/R = 0.67 at σ_N = 1.0, as the super-cavitation is extensively formed at r/R = 0.75 – 1.0 and the low pressure on the suction side is washed down to the trailing-edge region of the pressure side. The suction-side pressure distribution at σ_N = 1.0 shows that $-C_P \approx \sigma_N$ is extended to the trailing edge at r/R = 0.67 – 1.0.

The sectional pressure distribution on r/R = 0.97 in Figure 16 shows a suction surge at $x/C \leq 0.4$ at σ_N = 10.0, which contributes to the bounce-up of the declining loading. The sectional pressure distributions at σ_N = 1.763 show that the leading-edge pressure difference between the two sides is smaller on r/R = 0.97 than on r/R = 0.93, which accounts for the loading fall-off at r/R = 0.93 – 1.0.

As the cavity area over the blade surface is increased at low cavitation numbers, viscous shear stress is reduced at $r/R \geq 0.7$ as shown in Figure 13(b). However, the shear stress reduction is too small compared to that of the remaining pressure leading to thrust breakdown in extensive cavitation.

The sectional pressure distributions on r/R = 0.7 in Figure 17(a) show that the low pressure of $-C_P = \sigma_N$ on the suction side is extended to 0.25·C and the trailing edge at σ_N = 1.383 and 1.0, respectively, so the axial loading on r/R = 0.7 is higher at σ_N = 1.0 – 1.383 than at higher σ_N. The reductions of the leading-edge suction on the suction side and the trailing-edge pressure on the pressure side lead to lower axial loading in the region of r/R = 0.75 – 0.9 at σ_N = 1.0 than at higher σ_N in spite of the extension of the low-pressure region on the suction side aft of the mid-chord.

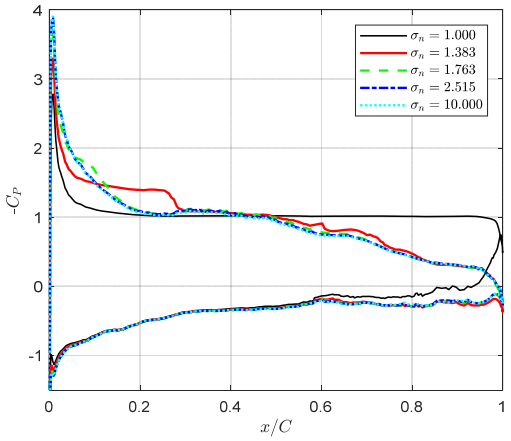

(a) r/R = 0.7

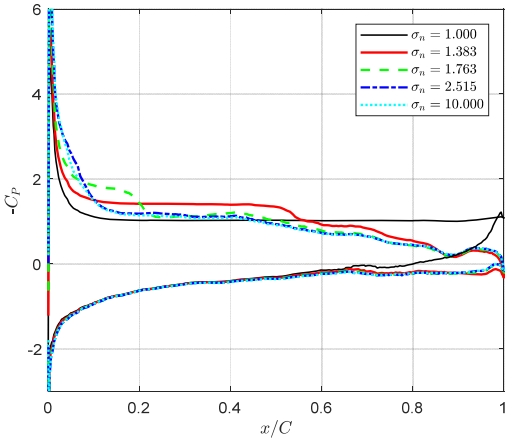

(b) r/R = 0.8

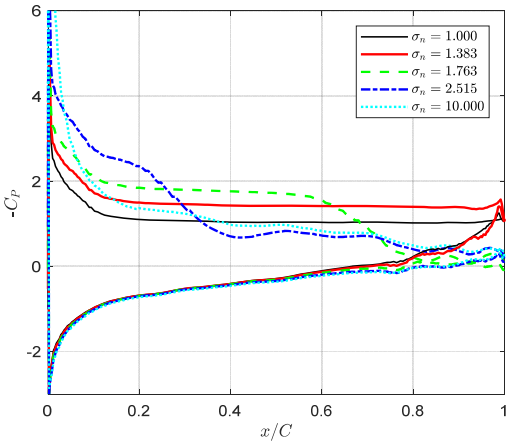

(c) r/R = 0.9

Figure 17: Sectional pressure distributions in CFD with varying cavitation number

6 CONCLUSION

CFD simulations are made on INSEAN E779A propeller with varying cavitation number for investigating propeller performance alterations in cavitating conditions. The comparison of the CFD and experimental results shows a reasonable agreement in the variations of cavity area, thrust and torque in moderate cavitation. Thrust and

torque breakdowns are shown at higher cavitation numbers and larger cavity areas in CFD than in the experiment, as the cavity extent is overestimated in CFD especially in extensive cavitation. Both the CFD and experimental results show that torque breakdown occurs in lower cavitation numbers than thrust breakdown, which leads to efficiency loss in excessively cavitating conditions. The CFD results show that the drop of the sectional loading in the region under super-cavitation leads to thrust breakdown, as the suction at the leading edge of the suction side and the pressure at the trailing edge of the pressure side are reduced in spite of the extension of the low-pressure region on the suction side aft of the mid-chord.

The transition model in CFD does not make significant differences in cavity extent at outer radii generally having fully turbulent flows in cavitation tunnel tests, but it is necessary for more accurate predictions of thrust and torque over the whole blade. As the CFD results show that the rates of cavitation bubble growth and collapse are changed depending on the seed density in cavitation model, it shows possibility to take into account the effects of cavitation tunnel water quality in CFD simulations in a simplified way by using the seed density.

REFERENCES

Bensow, R. E. & Bark, G. (2010). 'Simulating cavitating flows with LES in Openfoam'. Proceedings of 5th European Conference on Computational Fluid Dynamics, Lisbon, Portugal

Black, S. D. (2007). 'Thrust breakdown characteristics of conventional propellers'. Hydromechanics Department Report, Naval Surface Warfare Center Carderock Division, West Bethesda, MD, USA

Burrill, L. C. & Emerson, A. (1963). 'Propeller cavitation: further tests on 16 in. propeller models in the King's College cavitation tunnel'. Transactions of the North East Coast Institution of Engineers and Shipbuilders, vol. 79, Newcastle Upon Tyne, United Kingdom.

Kuiper, G. (1981). Cavitation inception on ship propeller models. Ph.D. Thesis, Wageningen: Netherlands Ship Model Basin

Lindau, J. W., Boger, D. A., Medvitz, R. B. & Kunz, R. F. (2005). 'Propeller cavitation breakdown analysis'. Journal of Fluids Engineering Vol. 127.

Paik, K., Park, H. & Seo, J. (2013). 'RANS simulation of cavitation and hull pressure fluctuation for marine propeller operating behind-hull condition'. Journal of Naval Architecture & Ocean Engineering 5(4)

Pereira, F., Salvatore, F. & Di Felice, F. (2004a). 'Measurement and modeling of propeller cavitation in uniform inflow'. Journal of Fluids Engineering Vol. 126.

Pereira, F. Salvatore, F., Di Felice, F. & Soave, M. (2004b). 'Experiment Investigation of a cavitating propeller in non-uniform inflow'. Proceedings of 25th Symposium on Naval Hydrodynamics, St. John's, Newfoundland, Canada

Salvatore, F. (2006). 'The INSEAN E779A Propeller Dataset'. INSEAN Technical Report, Rome: INSEAN

Schnerr, G. H. & Sauer, J. (2001). 'Physical and numerical modeling of unsteady cavitation dynamics'. Proceedings of 4th International Conference on Multiphase Flow (ICMF2001), New Orleans, LA, USA

Shin, K. W. & Andersen, P. (2015). 'CFD analysis of cloud cavitation on three tip-modified propellers with systematically varied tip geometry'. Proceedings of 9th International Symposium on Cavitation, Lausanne, Switzerland

Shin, K. W. & Andersen, P. (2018a). 'Numerical study on characteristics of cloud cavitation on a ship propeller'. Proceedings of 3rd International Meeting on Propeller Cavitation, Istanbul, Turkey

Shin, K. W. & Andersen, P. (2018b). 'CFD analysis of propeller tip vortex cavitation in ship wake fields'. Proceedings of 9th International Symposium on Cavitation (CAV2018), Baltimore, MD, USA

Shin, K. W., Regener, P. B. & Andersen, P. (2015). 'Methods for cavitation prediction on tip-modified propellers in ship wake fields'. Proceedings of 4th International Symposium on Marine Propulsors (SMP'15), Austin, TX, USA

Vaz, G., Hally, D., Huuva, T., Bulten, N., Muller, P., Becchi, P., Herrer, J. L. R., Whitworth, S., Mace, R. & Korsstrom, A. (2015). 'Cavitating flow calculations for the E779A propeller in open water and behind conditions'. Proceedings of 4th International Symposium on Marine Propulsors (SMP'15), Austin, TX, USA

Yilmaz, N., Atlar, M. & Fitzsimmons, P. A. (2018). 'An improved tip vortex cavitation model for propeller-rudder interaction'. Proceedings of 10th International Symposium on Cavitation (CAV2018), Baltimore, MD, USA